Recursive SISO Impedance Modeling of Single-Phase Voltage Source Rectifiers

Document license:
TAVERNE

DOI:
10.1109/TPEL.2021.3103849

Document status and date:
Published: 01/02/2022

Document Version:
Publisher's PDF, also known as Version of Record (includes final page, issue and volume numbers)

Please check the document version of this publication:

• A submitted manuscript is the version of the article upon submission and before peer-review. There can be important differences between the submitted version and the official published version of record. People interested in the research are advised to contact the author for the final version of the publication, or visit the DOI to the publisher's website.
• The final author version and the galley proof are versions of the publication after peer review.
• The final published version features the final layout of the paper including the volume, issue and page numbers.

Link to publication

Recursive SISO Impedance Modeling of Single-Phase Voltage Source Rectifiers

Jianheng Lin ©, Mei Su ©, *Member, IEEE*, Yao Sun ©, *Member, IEEE*, Dongsheng Yang ©, *Senior Member, IEEE*, and Shiming Xie ©

Abstract—Due to the nonlinear time-periodic nature, precise impedance modeling of power-converter-based single-phase ac systems is complex. Small-signal modeling for the systems with a fixed operating point is easy, but the extension of the same procedure to the systems with time-periodic trajectory is still challenging. In this article, a recursive single-input single-output (SISO) impedance modeling framework for single-phase rectifiers is presented, which can greatly simplify both the modeling procedure and the resulting impedance model. A general linear-time periodic modeling method is proposed by extending the linear-time invariant modeling method, where frequency-coupling effects are modeled by the transfer function vector rather than the transfer function matrix, so the modeling complexity is reduced. Furthermore, based on the idea of mathematical induction, an analytical and accurate recursive SISO impedance model is derived. The resulting recursive SISO impedance model can characterize the frequency-coupling dynamics of arbitrary order with a low computation burden. Experiments validate the accuracy of the recursive SISO impedance modeling method.

Index Terms—Impedance, linear-time periodic (LTP) modeling, single-input single-output (SISO), single-phase converter.

I. INTRODUCTION

OVER the past decades, voltage source converters (VSCs) are being widely used in power grids, such as distributed generation, electric railway traction, and flexible power transmission [1]–[3]. With the increasing penetration of VSCs in power system, it not only improves efficiency and enhances control flexibility, but also leads to some stability issues introduced by the dynamic interactions between power converters and passive components (e.g., power filters and the grid impedance) [4], [5].

Many research efforts have thus been made to deal with VSC-grid interactions. It has been reported that the frequency coupling effect (FCE) widely exists in the VSC systems, whose generation reasons include the phase-locked loop(PLL), asymmetric controllers, and so on [2], [4]. The FCE implies that there is coupling between different frequency components. Different system structures lead to different numbers of frequency coupling components. The frequency coupling components will form additional sideband loops, which poses serious challenges to accurate impedance modeling.

For three-phase balanced VSC systems, the number of frequency couplings is typically bounded by two [4]–[6]. In order to incorporate the coupling dynamics, the three-phase VSC is modeled as a 2×2 impedance matrix either in the dq synchronous rotating frame [7] or in the $\alpha\beta$ stationary frame [8]. In dq frame, the VSC system is linearized at constant dc operating points, leading to a linear-time invariant (LTI) system. If performing linearization in the stationary frame, the resulting model is linear-time periodic (LTP). Linearizing in different reference frames yields different types of impedance (i.e., dq impedance, phasor impedance, and sequence impedance), and the correlation among different models are unveiled in [9] and [10]. On this basis, many detailed impedance models including different factors are formulated, e.g., constant power load [11] and PLL [12], [13]. Based on the complex vector notation [14] or algebraic calculation [15], the multiple-input multiple-output (MIMO) impedance matrix can be simplified into a single-input single-output (SISO) impedance model. The SISO impedance model not only facilitates the understanding of the consequence of impedance measurement under frequency couplings, but also provides an intuitive insight into the interactions among VSCs and power grids [16], [17].

However, in either three-phase unbalanced or single-phase systems, the time-periodic nature of the system introduces an infinite number of frequency couplings, which greatly complicates the modeling. Besides, the LTI modeling is no longer suitable because of the time-periodic operating trajectory. Based on the above considerations, the LTP framework-based modeling approaches are more feasible for the impedance modeling of such systems.

Generally speaking, there have been two general multifrequency modeling methods capable of dealing with time-periodic systems. The generalized averaging modeling (GAM) was earlier introduced to capture the cross-coupling dynamics in [18] by Sanders *et al.*, which is also known as dynamic phasor

modeling [19], [20]. The key of GAM is to decompose the actual time-periodic waveform into the phasors in different frequency domains based on the harmonic balance principle. On the other hand, the harmonic-state space (HSS) modeling method, which was first proposed by Wereley in [21], has been widely applied to address harmonic stability issues by Kwon *et al.* in [22] and [23] and by Salis *et al.* in [24] and [25]. Moreover, the counterpart of the HSS in the frequency domain is called as harmonic transfer function (HTF) approach [26], which directly establishes the harmonic impedance model in the frequency domain [2], [27], [28]. The core idea of HSS/HTF lies in the introduction of the exponential modulated periodic signal, which maps the LTP model as an infinite-dimensional LTI model. The models obtained from GAM or HSS/HTF are characterized by MIMO with infinite dimensions, bringing about significant complexity to stability analysis and physical measurement.

In order to simplify the MIMO model, many efforts have been devoted to SISO equivalent impedance modeling method. Harmonic linearization, proposed by Sun *et al.* in [29], gives the describing-function-based model. However, the neglect of cross-coupling dynamics limits its accuracy, especially in the low-frequency regions [30]. The harmonic signal-flow graph method is proposed to streamline and visualize the modeling process of harmonic linearization by Shah *et al.* in [31] and [32]. The additional loops closed through the grid impedance are not been considered. In [33], Qian *et al.* derive a single-frequency impedance model, incorporating the effect of the other two frequency-coupling components. This incorporation does improve the accuracy of the model; it is still inadequate to predict the impact of certain factors, such as the modulation method. The latest work in [34], presented by Zhang *et al.*, extends the model to include coupling components of arbitrary order by the HTF method. However, the developed SISO impedance model is represented by a series of large-dimensional matrices, which degrades model analyticity and increases computation time.

Besides the model simplification, another obstacle is the modeling complexity. In the describing function-based methods, the concept of perturbation injection is used for submodule modeling [29]–[32]. To solve the multiplication of injected perturbation and time-periodic gain, complex convolution is required. Moreover, the form of perturbations needs to be defined empirically. Considering more perturbations increase the modeling complexity while considering fewer perturbations degrade the model accuracy. As for the HTF modeling, each control loop of the VSC is modeled separately as a Toeplitz matrix, and then the models are combined based on their interconnections [26]–[28], [34]. In the modeling process, a series of matrix operations are required, especially the matrix inversion, which significantly increases the modeling complexity. Note that each row/column of the Toeplitz matrix can be obtained by frequency shifting another row/column. This observation implies that the information of the Toeplitz matrix is redundant in describing the FCEs.

In order to address the abovementioned challenges, a recursive SISO impedance modeling framework for single-phase voltage source rectifiers (VSRs) is proposed in this article. The main contributions of the article are summarized as follows.

1) A general and simple LTP modeling method is proposed by extending the LTI modeling. It does not require complex convolution and large-dimensional matrix operations for the submodule modeling. Therefore, the modeling complexity is reduced.
2) The recursive SISO impedance model is analytical and easy to include harmonics of arbitrary order based on the required model accuracy. Compared with the HTF-based SISO model [34], the recursive SISO impedance model avoids complicated matrix inversion.

The rest of this article is organized as follows. In Section II, the basic procedures of the LTP modeling approach are introduced. In Section III, the single-phase VSR system configuration is described. Section IV presents the harmonic admittance modeling under no grid impedance. In Section V, the recursive SISO impedance model is derived and a detailed comparison with other existing models is given. In Section VI, the developed impedance model is validated by experiments in terms of impedance measurement and stability analysis. Finally, Section VII concludes this article.

II. FROM LTI MODELING TO LTP MODELING

The information contained in the Toeplitz matrix is redundant, which increases the modeling complexity. In fact, one row/column of the Toeplitz matrix is enough to represent the complete system model. In the light of this observation, a simple LTP modeling is introduced as follows.

A. LTI Modeling Revisit

To better understand the LTP modeling, a brief revisit of LTI modeling is given first. Consider a one-dimensional nonlinear time-invariant system

$$\frac{dx}{dt} = f(x, u) \tag{1}$$

where $x \in \mathbb{R}$ and $u \in \mathbb{R}$ represent a state variable and an input variable, respectively, and f is a nonlinear function from $\mathbb{R}^2$ to $\mathbb{R}$.

This system is autonomous, and its small-signal model can be derived as

$$\frac{d\tilde{x}}{dt} = \left.\frac{\partial f}{\partial x}\right|_{x=\bar{x}, u=\bar{u}} \cdot \tilde{x} + \left.\frac{\partial f}{\partial u}\right|_{x=\bar{x}, u=\bar{u}} \cdot \tilde{u} := \alpha \cdot \tilde{x} + \beta \cdot \tilde{u} \tag{2}$$

where the superscripts "~" and "–" represent the small-signal and steady-state quantities, respectively. Both α and β are constant values determined by the steady-state operating points.

Applying Laplace transform to (2), it gives that

$$s \cdot \tilde{x}(s) = \alpha \cdot \tilde{x}(s) + \beta \cdot \tilde{u}(s) \tag{3}$$

where $s = j\omega$ and ω denotes the frequency variable.

Then, the transfer function from input to state is obtained as

$$G(s) = \frac{\tilde{x}(s)}{\tilde{u}(s)} = \frac{\beta}{s - \alpha}. \tag{4}$$

By repeating the operations from (1) to (4), the small-signal model of a nonlinear time-invariant system in the frequency domain can be derived.

B. LTP Modeling Approach

The dynamics of a one-dimensional nonlinear time-periodic system is described as

$$\frac{dx}{dt} = f\left(x\left(t\right), u\left(t\right)\right) \tag{5}$$

with its periodicity T_0 as

$$\begin{cases} \bar{x}\left(t\right) = \bar{x}\left(t + T_0\right) \\ \bar{u}\left(t\right) = \bar{u}\left(t + T_0\right). \end{cases} \tag{6}$$

The model of the single-phase grid-connected system is a typical example of this kind because of the steady-state time-periodic operating trajectories.

The linearized model of such a nonautonomous system is

$$\frac{d\tilde{x}}{dt} = \left.\frac{\partial f}{\partial x}\right|_{\substack{x(t)=\bar{x}(t) \\ u(t)=\bar{u}(t)}} \cdot \tilde{x} + \left.\frac{\partial f}{\partial u}\right|_{\substack{x(t)=\bar{x}(t) \\ u(t)=\bar{u}(t)}} \cdot \tilde{u}$$

$$:= \alpha\left(t\right) \cdot \tilde{x} + \beta\left(t\right) \cdot \tilde{u} \tag{7}$$

where $\alpha(t)$ and $\beta(t)$ are determined by the steady-state operating trajectories $\bar{x}(t)$ and $\bar{u}(t)$, satisfying

$$\begin{cases} \alpha\left(t\right) = \alpha\left(t + T_0\right) \\ \beta\left(t\right) = \beta\left(t + T_0\right). \end{cases} \tag{8}$$

As observed from (7), it is not able to derive the transfer function from the input to the state directly due to the time-periodic coefficients.

According to the Fourier transform theory, periodic signals satisfying Dirichlet conditions could be represented by a complex exponential series of infinite dimensions [35]. Thus, (8) can be rewritten by the Fourier series as

$$\alpha\left(t\right) = \sum_{k=-\infty}^{\infty} a_k e^{jk\omega_0 t}, \; (k \in \mathbb{Z}) \tag{9}$$

$$\beta\left(t\right) = \sum_{k=-\infty}^{\infty} b_k e^{jk\omega_0 t}, \; (k \in \mathbb{Z}) \tag{10}$$

where $\omega_0 = 2\pi/T_0$. And a_k and b_k are complex Fourier coefficients, which are given by

$$a_k = \frac{1}{T_0} \int_0^{T_0} \alpha\left(t\right) e^{-jk\omega_0 t} dt \tag{11}$$

$$b_k = \frac{1}{T_0} \int_0^{T_0} \beta\left(t\right) e^{-jk\omega_0 t} dt. \tag{12}$$

Substituting (9) and (10) into (7) yields

$$\frac{d\tilde{x}}{dt} = \left[\sum_{k=-\infty}^{\infty} a_k e^{jk\omega_0 t}\right] \cdot \tilde{x} + \left[\sum_{k=-\infty}^{\infty} b_k e^{jk\omega_0 t}\right] \cdot \tilde{u}. \tag{13}$$
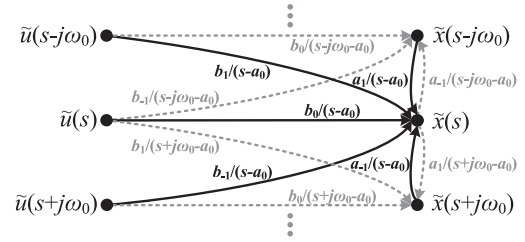

Fig. 1. Harmonic signal-flow graph of the time-periodic system.

Then, according to the displacement property of the Laplace transform, the frequency domain expression of (13) is

$$s\tilde{x}\left(s\right) = \left[\sum_{k=-\infty}^{\infty} a_k \tilde{x}\left(s - jk\omega_0\right)\right]$$

$$+ \left[\sum_{k=-\infty}^{\infty} b_k \tilde{u}\left(s - jk\omega_0\right)\right]. \tag{14}$$

It is found that $\tilde{x}$ at a given frequency ω is related to $\tilde{x}$ and $\tilde{u}$ not only at frequency ω, but also multiple sideband frequencies $\omega \pm k\omega_0$ ($k \in \mathbb{Z}$). This proves the existence of the frequency-coupling effect in the time-periodic systems.

It is worth noting that (14) corresponds to one row of the Toeplitz matrix of the LTP system. Moreover, due to the arbitrariness of s, another row can be easily derived by frequency shifting as

$$(s - jm\omega_0)\,\tilde{x}\left(s - jm\omega_0\right)$$

$$= \left[\sum_{k=-\infty}^{\infty} a_k \tilde{x}\left(s - j\left(m + k\right)\omega_0\right)\right]$$

$$+ \left[\sum_{k=-\infty}^{\infty} b_k \tilde{u}\left(s - j\left(m + k\right)\omega_0\right)\right]. \tag{15}$$

By applying the frequency-shifting operation on (14) repeatedly, the frequency response from input to any order of harmonic can be constructed. The total dynamic propagations of the LTP system in the frequency domain are shown in Fig. 1.

In this way, the use of matrix operation can be avoided and complex convolution is not required. Thus, the modeling complexity can be reduced. Also, the number of frequency-shifting operations required depends on the number of nonzero Fourier coefficients. In the practical analysis, truncation is usually required and the truncation order depends on the required accuracy [34]. By solving the obtained frequency-shifting equations, the SISO transfer function from $\tilde{u}(s)$ to $\tilde{x}(s)$ with consideration of frequency-coupling effects can be derived.

III. SYSTEM CONFIGURATION

The circuit configuration and control scheme of the studied single-phase VSR are depicted in Fig. 2. The main circuit is comprised of a power supply u_g, a grid impedance L_g/R_g, an input inductance L_f in series with a resistance R_f, an H-bridge circuit, an output capacitance C_{dc}, and a load resistance R_{dc}.
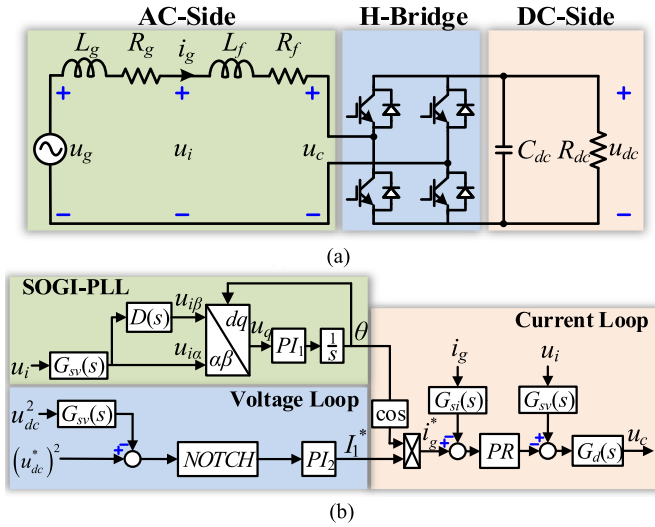
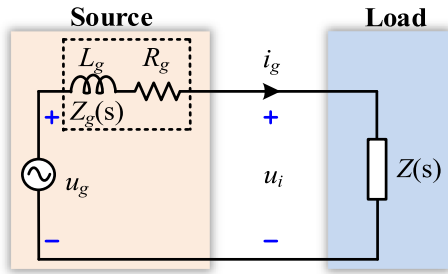Fig. 2. Schematic of a single-phase VSR system. (a) Main circuit. (b) Control diagram.

Fig. 3. Thevenin model of a single-phase VSR.

In the control diagram, a second-order generalized integrator (SOGI)-PLL is used to obtain the phase θ of the point of common coupling (PCC) voltage u_i. And the dc-link voltage u_{dc} and input current i_g are regulated by a voltage loop and a current loop, respectively.

The studied system is split into two subsystems at PCC: one is the source subsystem and the other is the load subsystem, as shown in Fig. 3. The analysis of source and load systems can separately bring to an impedance-based representation for both of them. Based on the input impedance $Z(s)$ and the grid impedance $Z_g(s)$, the impedance-based stability criteria can be applied to determine the system stability.

In this system, the sampling delay is modeled as

$$G_{si}(s) = \frac{1}{1 + s/\omega_i} \tag{16}$$

$$G_{sv}(s) = \frac{1}{1 + s/\omega_v} \tag{17}$$

where ω_i and ω_v are the cutoff frequency of anti-aliasing filters for current and voltage measurement, respectively.

Besides, an SOGI, a notch filter (NOTCH), two proportional-integral (PI) regulators, and a proportional-resonant (PR) regulator are given as

$$D(s) = \frac{2\xi\omega_1^2}{s^2 + 2\xi\omega_1 s + \omega_1^2} \tag{18}$$

$$\text{NOTCH}(s) = \frac{s^2 + \omega_n^2}{s^2 + \sigma s + \omega_n^2} \tag{19}$$

$$\text{PI}_m(s) = k_{pm} + \frac{k_{im}}{s} \quad (m = 1, 2) \tag{20}$$

$$\text{PR}(s) = k_{pc} + \frac{k_{rc}s}{s^2 + \omega_1^2} \tag{21}$$

where ω_1 is the angular frequency of the grid, ξ is the damping ratio, σ is bandwidth coefficient, ω_n is the center frequency, k_{pm} and k_{im} ($m = 1, 2$) are the PI controller parameters, and k_{pc} and k_{rc} are the PR controller parameters.

Zero-order hold effects and calculation delays are taken into consideration as

$$G_d(s) = e^{-sT_s} \frac{1 - e^{-sT_s}}{sT_s} \tag{22}$$

where T_s is the control period.

IV. HARMONIC ADMITTANCE MODELING

A. SOGI-PLL Modeling

The SOGI-PLL is used to track the phase θ of the PCC voltage u_i, which is used for generating current reference. The SOGI generates the $\pi/4$-delay signal $u_{i\beta}$ of $u_{i\alpha}$. Then, applying the Park transformation to $u_{i\alpha}$ and $u_{i\beta}$, the q axis voltage u_q is obtained

$$u_q(t) = -\sin[\theta(t)] u_{i\alpha}(t) + \cos[\theta(t)] u_{i\beta}(t). \tag{23}$$

Perturbing the variables in the time-domain, the linearized form of (23) is derived as

$$\tilde{u}_q(t) = -\sin(\omega_1 t)\tilde{u}_{i\alpha}(t) + \cos(\omega_1 t)\tilde{u}_{i\beta}(t) - V_1\tilde{\theta}(t) \tag{24}$$

where $\omega_1 t$ and V_1 are denoted as the phase and amplitude of the PCC voltage in steady-state, respectively.

According to (13) and (14), (24) can be rewritten as

$$\tilde{u}_q(s) = \frac{j}{2}[\tilde{u}_{i\alpha}(s - j\omega_1) - \tilde{u}_{i\alpha}(s + j\omega_1)]$$
$$+ \frac{1}{2}[\tilde{u}_{i\beta}(s - j\omega_1) + \tilde{u}_{i\beta}(s + j\omega_1)] - V_1\tilde{\theta}(s). \tag{25}$$

Based on the SOGI-PLL diagram, the following relationships hold:

$$\tilde{u}_{i\alpha}(s) = G_{sv}(s)\tilde{u}_i(s) \tag{26}$$

$$\tilde{u}_{i\beta}(s) = D(s)G_{sv}(s)\tilde{u}_i(s) \tag{27}$$

$$\tilde{\theta}(s) = H_{PLL}(s)\tilde{u}_q(s) \tag{28}$$

where $H_{PLL}(s) = \text{PI}_1(s)/s$.

Substituting (26)–(28) into (25), it is deduced that

$$\tilde{\theta}(s) = G_{PLL\_n}(s)\tilde{u}_i(s - j\omega_1) + G_{PLL\_p}(s)\tilde{u}_i(s + j\omega_1) \tag{29}$$

where

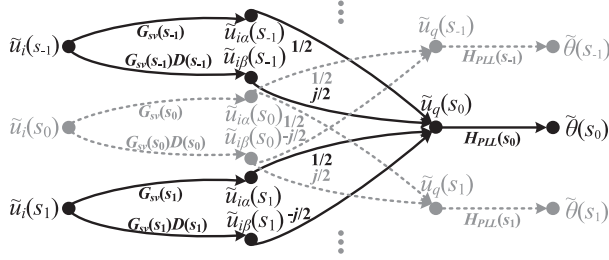$$G_{PLL\_n}(s) = G_{PLL}(s)G_{sv}(s - j\omega_1)[D(s - j\omega_1) + j] \tag{30}$$

Fig. 4. Harmonic signal-flow graph of the SOGI-PLL.

Fig. 5. Harmonic signal-flow graph of the voltage loop.

$$G_{\text{PLL}\_p}(s) = G_{\text{PLL}}(s) G_{\text{sv}}(s+j\omega_1)[D(s+j\omega_1)-j] \quad (31)$$

$$G_{\text{PLL}}(s) = \frac{H_{\text{PLL}}(s)}{2[1+V_1 H_{\text{PLL}}(s)]}. \quad (32)$$

Applying the frequency shifting to (25)–(28) by $\pm k\omega_1$ ($k \in \mathbb{Z}$), the harmonic signal-flow graph of the SOGI-PLL is drawn as Fig. 4, where s_k is defined as $s + jk\omega_1$ ($k \in \mathbb{Z}$). It is observed that the perturbed phase $\tilde{\theta}$ at a given frequency ω is related to the PCC voltage $\tilde{u}_{\text{i}}$ at the two coupled frequencies $\omega \pm \omega_1$.

B. Voltage Loop Modeling

Assume that the power losses on the switches of the rectifier are neglectable, the power relationship between the ac side and the dc side in Fig. 2(a) can be described as

$$\frac{C_{\text{dc}}}{2} \frac{du_{\text{dc}}^2(t)}{dt} + \frac{u_{\text{dc}}^2(t)}{R_{\text{dc}}}$$
$$= u_i(t) i_g(t) - \frac{L_f}{2} \frac{di_g^2(t)}{dt} - R_f i_g^2(t). \quad (33)$$

Linearizing (33) gives (34) shown at the bottom of this page, and its corresponding frequency domain expression is obtained as (35) shown at the bottom of this page. I_1 and φ_{i1} correspond to the magnitude and initial phase of the fundamental current in steady-state, respectively. And $G_L(s)$, $G_{x1}(s)$, and $G_{x2}(s)$ are given by

$$G_L(s) = \frac{R_{\text{dc}}}{C_{\text{dc}} R_{\text{dc}} s + 2} \quad (36)$$

$$G_{x1}(s) = V_1 - (s - j\omega_1) L_f I_1 e^{j\varphi_{i1}}$$
$$- j\omega_1 L_f I_1 e^{j\varphi_{i1}} - 2R_f I_1 e^{j\varphi_{i1}} \quad (37)$$

$$G_{x2}(s) = V_1 - (s + j\omega_1) L_f I_1 e^{-j\varphi_{i1}}$$
$$+ j\omega_1 L_f I_1 e^{-j\varphi_{i1}} - 2R_f I_1 e^{-j\varphi_{i1}}. \quad (38)$$

From Fig. 2, the perturbed output of the voltage loop is

$$\tilde{I}_1^*(s) = -H_v(s) \tilde{u}_{\text{dc}}^2(s) \quad (39)$$

where

$$H_v(s) = PI_2(s) \text{NOTCH}(s) G_{\text{sv}}(s). \quad (40)$$

Based on the above calculations, the harmonic signal-flow graph of the voltage loop can be drawn as Fig. 5. In the voltage loop, $\tilde{I}_1^*$ at a given frequency ω is dependent on $\tilde{u}_i$ and $\tilde{i}_g$ at two coupled frequencies $\omega \pm \omega_1$.

C. Current Loop Modeling

The grid current reference is

$$i_g^*(t) = I_1^*(t) \cos[\theta(t)]. \quad (41)$$

The corresponding small-signal form of (41) is given as

$$\tilde{i}_g^*(t) = -I_1 \sin(\omega_1 t) \tilde{\theta}(t) + \cos(\omega_1 t) \tilde{I}_1^*(t). \quad (42)$$

In the frequency domain, (42) is rewritten as

$$\tilde{i}_g^*(s) = \frac{jI_1}{2} \left[\tilde{\theta}(s - j\omega_1) - \tilde{\theta}(s + j\omega_1) \right]$$
$$+ \frac{1}{2} \left[\tilde{I}_1^*(s - j\omega_1) + \tilde{I}_1^*(s + j\omega_1) \right]. \quad (43)$$

Due to the current regulator, the perturbed converter voltage including the feedforward term is

$$\tilde{u}_c(s) = G_d(s) \left\{ \begin{array}{l} G_{\text{sv}}(s) \tilde{u}_i(s) \\ -PR(s) [\tilde{i}_g^*(s) - G_{\text{si}}(s) \tilde{i}_g(s)] \end{array} \right\}. \quad (44)$$

Similarly, cross-coupling dynamics exist in the current loop that $\tilde{i}_g^*$ at a given frequency ω is coupled with $\tilde{\theta}$ and $\tilde{I}_1^*$ at two coupled frequencies $\omega \pm \omega_1$. And the harmonic signal-flow graph of the current loop is depicted as Fig. 6.

D. Harmonic Admittance Modeling

The harmonic signal-flow graphs show that the single-phase VSR system is a MIMO system essentially, which is different

$$\frac{C_{\text{dc}}}{2} \frac{d\tilde{u}_{\text{dc}}^2(t)}{dt} + \frac{\tilde{u}_{\text{dc}}^2(t)}{R_{\text{dc}}} = [V_1 \cos(\omega_1 t) + \omega_1 L_f I_1 \sin(\omega_1 t + \varphi_{i1})] \tilde{i}_g(t) + I_1 \cos(\omega_1 t + \varphi_{i1}) \left[\tilde{u}_i(t) - L_f \frac{d\tilde{i}_g(t)}{dt} - 2R_f \tilde{i}_g(t) \right] \quad (34)$$

$$\tilde{u}_{\text{dc}}^2(s) = G_L(s) \left[G_{x1}(s) \tilde{i}_g(s - j\omega_1) + I_1 e^{j\varphi_{i1}} \tilde{u}_i(s - j\omega_1) + G_{x2}(s) \tilde{i}_g(s + j\omega_1) + I_1 e^{-j\varphi_{i1}} \tilde{u}_i(s + j\omega_1) \right] \quad (35)$$
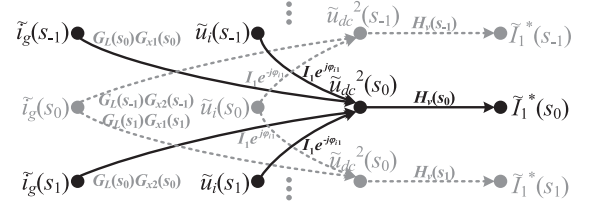
Fig. 6. Harmonic signal-flow graph of the current loop.

Fig. 7. Fundamental frequency coupling relationship of the single-phase VSR under no grid impedance.

from the usual time-invariant system. According to the above analysis, it is worth noting that different signal-flow paths are translated copies of each other with frequency shifting proportional to the fundamental frequency ω_1. Therefore, the system model can be extended to include harmonics of arbitrary order by frequency-shifting any one signal-flow path without complicated calculations.

The current dynamics in the average model is

$$(L_f s + R_f)\tilde{i}_g(s) = \tilde{u}_i(s) - \tilde{u}_c(s). \tag{45}$$

Substituting (29), (39), and (44) into (45), the dynamics between voltage and current at PCC is derived as (46) shown at the bottom of this page, where $G_{i,-2}(s)$, $G_{i,0}(s)$, $G_{i,2}(s)$, $G_{u,-2}(s)$, $G_{u,0}(s)$, and $G_{u,2}(s)$ are given in Appendix.

Neglecting the coupling terms in (44), the conventional input impedance is obtained as

$$Z_c(s) = \frac{G_{i,0}(s)}{G_{u,0}(s)}. \tag{47}$$

In order to include the interactions among different frequency domains, frequency-shifting (46) to $s \pm j2\omega_1$ gives

$$\tilde{i}_g(s - j2\omega_1)$$
$$= \frac{G_{u,2}(s - j2\omega_1)\tilde{u}_i(s) - G_{i,2}(s - j2\omega_1)\tilde{i}_g(s)}{G_{i,0}(s - j2\omega_1)} \tag{48}$$

$$\tilde{i}_g(s + j2\omega_1)$$
$$= \frac{G_{u,-2}(s + j2\omega_1)\tilde{u}_i(s) - G_{i,-2}(s + j2\omega_1)\tilde{i}_g(s)}{G_{i,0}(s + j2\omega_1)} \tag{49}$$

where only the perturbed voltage term $\tilde{u}_i(s)$ is retained due to no grid impedance and the harmonic currents with quadruple line frequency deviation are assumed to be zero.

Substituting (48) and (49) into (46), the input impedance with capturing FCEs under no grid impedance is derived as (50) shown at the bottom of this page.

Substituting (50) into (48) and (49), the harmonic admittances are derived as

$$Y_n(s) = \frac{\tilde{i}_g(s - j2\omega_1)}{\tilde{u}_i(s)}$$
$$= \frac{G_{u,2}(s - j2\omega_1) - G_{i,2}(s - j2\omega_1)Y_{\mathrm{op}}(s)}{G_{i,0}(s - j2\omega_1)} \tag{51}$$

$$Y_p(s) = \frac{\tilde{i}_g(s + j2\omega_1)}{\tilde{u}_i(s)}$$
$$= \frac{G_{u,-2}(s + j2\omega_1) - G_{i,-2}(s + j2\omega_1)Y_{\mathrm{op}}(s)}{G_{i,0}(s + j2\omega_1)} \tag{52}$$

where $Y_{\mathrm{op}}(s) = 1/Z_{\mathrm{op}}(s)$.

The small-signal modeling illustrates that a perturbed PCC voltage $\tilde{u}_i$ at a given frequency ω will generate three harmonic grid currents $\tilde{i}_g$ at the frequencies ω and $\omega \pm \omega_1$, as depicted in Fig. 7. The existence of the FCE described by (51) and (52) poses a challenge to the modeling of the VSC-grid interaction.

V. RECURSIVE SISO IMPEDANCE MODELING AND ANALYSIS

When there is a grid impedance on the grid side, the harmonic currents would generate the voltage at the same frequency and thus constitute additional feedback loops. The multifrequency diagram of a single-phase VSR with the additional closed loops is depicted in Fig. 8. The additional loops are the translated copies of the fundamental loop (denoted by the black line) with frequency shifting $\pm k\omega_1$. Moreover, the order of harmonic would extend to infinite at the presence of the grid impedance.

A. Recursive SISO Impedance Modeling

According to Fig. 8, the relationship between $\tilde{i}_g$ and $\tilde{u}_i$ in different frequency domains can be consistently established as

$$\tilde{i}_g(s_K) = Y_p(s_{K-2})\tilde{u}_i(s_{K-2}) + Y_{\mathrm{op}}(s_K)\tilde{u}_i(s_K)$$
$$+ Y_n(s_{K+2})\tilde{u}_i(s_{K+2}) \tag{53}$$

$$G_{i,-2}(s)\tilde{i}_g(s - j2\omega_1) + G_{i,0}(s)\tilde{i}_g(s) + G_{i,2}(s)\tilde{i}_g(s + j2\omega_1)$$
$$= G_{u,-2}(s)\tilde{u}_i(s - j2\omega_1) + G_{u,0}(s)\tilde{u}_i(s) + G_{u,2}(s)\tilde{u}_i(s + j2\omega_1) \tag{46}$$

$$Z_{\mathrm{op}}(s) = \frac{G_{i,0}(s) - G_{i,2}(s - j2\omega_1)G_{i,-2}(s)/G_{i,0}(s - j2\omega_1) - G_{i,2}(s)G_{i,-2}(s + j2\omega_1)/G_{i,0}(s + j2\omega_1)}{G_{u,0}(s) - G_{i,-2}(s)G_{u,2}(s - j2\omega_1)/G_{i,0}(s - j2\omega_1) - G_{i,2}(s)G_{u,-2}(s + j2\omega_1)/G_{i,0}(s + j2\omega_1)} \tag{50}$$
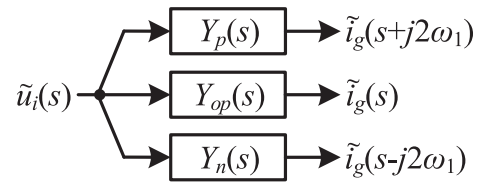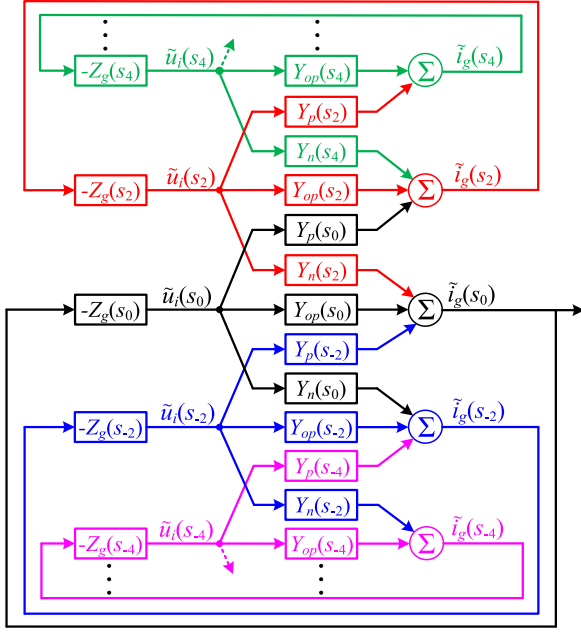
Fig. 8. Multifrequency diagram of the single-phase VSR considering the grid impedance.
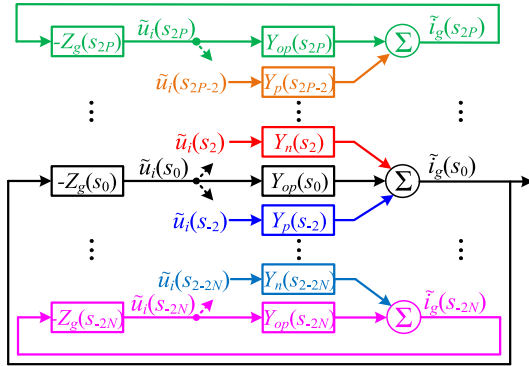

Fig. 9. Truncated multifrequency diagram with P positive loops and N negative loops.

where $K \in \mathbb{Z}$. In addition, due to the existence of grid impedance, it is established that

$$\tilde{i}_g (s_K) = -Y_g (s_K) \tilde{u}_i (s_K) \tag{54}$$

where $K \in \mathbb{Z} \backslash 0$.

In order to obtain a model that is suitable for analysis, truncation is required. Assume that the multiloop system is truncated to P ($P \in \mathbb{N}$) positive loops and N ($N \in \mathbb{N}$) negative loops as depicted

in Fig. 9, the truncation conditions are expressed as

$$\begin{cases} \tilde{u}_i (s_{2X}) = 0, & X \geq P + 1 \\ \tilde{u}_i (s_{-2Y}) = 0, & Y \geq N + 1 \end{cases} \tag{55}$$

where $X \in \mathbb{N}$ and $Y \in \mathbb{N}$.

The positive loop truncation is taken as an example to illustrate how to obtain a truncated model. Based on the idea of mathematical induction, assume first that

$$Y_n (s_{2X}) \tilde{u}_i (s_{2X}) = F_P (P - (X - 1)) \tilde{u}_i (s_{2(X-1)}) \tag{56}$$

where $1 \leq X \leq P + 1$, $F_P(P - (X - 1))$ is a mapping function from $\tilde{u}_i(s_{2(X-1)})$ to $\tilde{u}_i(s_{2X})$ that needs to be determined, and $F_P(0) = 0$.

Next, replacing K in (53) with $2X$ gives

$$\tilde{i}_g (s_{2X}) = Y_p (s_{2(X-1)}) \tilde{u}_i (s_{2(X-1)}) + Y_{\mathrm{op}} (s_{2X}) \tilde{u}_i (s_{2X})$$
$$+ Y_n (s_{2(X+1)}) \tilde{u}_i (s_{2(X+1)}) . \tag{57}$$

Combining (54) and (56) into (57), it is obtained as

$$Y_n (s_{2X}) \tilde{u}_i (s_{2X})$$
$$= \frac{-Y_n (s_{2X}) Y_p (s_{2(X-1)})}{Y_g (s_{2X}) + Y_{\mathrm{op}} (s_{2X}) + F_P (P - X)} \tilde{u}_i (s_{2(X-1)}) . \tag{58}$$

Comparing (56) and (58), $F_P(\bullet)$ can be solved as (59), shown at the bottom of this page.

In the same way, a recursive relationship for the negative loop truncation can be derived as

$$Y_p (s_{-2Y}) \tilde{u}_i (s_{-2Y}) = F_N (N - (Y - 1)) \tilde{u}_i (s_{-2(Y-1)}) \tag{60}$$

where $1 \leq Y \leq N + 1$, $F_N(\bullet)$ is given as (61), shown at the bottom of this page.

Finally, substituting $X = 1$ into (56) and substituting $Y = 1$ into (60) yield

$$Y_n (s_2) \tilde{u}_i (s_2) = F_P (P) \tilde{u}_i (s_0) \tag{62}$$

$$Y_p (s_{-2}) \tilde{u}_i (s_{-2}) = F_N (N) \tilde{u}_i (s_0) . \tag{63}$$

Substituting $K = 0$ into (53) gives

$$\tilde{i}_g (s_0) = Y_p (s_{-2}) \tilde{u}_i (s_{-2}) + Y_{\mathrm{op}} (s_0) \tilde{u}_i (s_0)$$
$$+ Y_n (s_2) \tilde{u}_i (s_2) . \tag{64}$$

Combining (62)–(64), a recursive SISO impedance model can be derived as

$$Z (s) = \frac{\tilde{u}_i (s_0)}{\tilde{i}_g (s_0)} = \frac{1}{Y_{\mathrm{op}} (s) + F_N (N) + F_P (P)} . \tag{65}$$

$$F_P (p) = \frac{-Y_n (s_{2(P-p+1)}) Y_p (s_{2(P-p)})}{Y_g (s_{2(P-p+1)}) + Y_{op} (s_{2(P-p+1)}) + F_P (p - 1)} \text{ with } F_P (0) = 0 \tag{59}$$

$$F_N (n) = \frac{-Y_p (s_{-2(N-n+1)}) Y_n (s_{-2(N-n)})}{Y_g (s_{-2(N-n+1)}) + Y_{op} (s_{-2(N-n+1)}) + F_N (n - 1)} \text{ with } F_N (0) = 0 \tag{61}$$
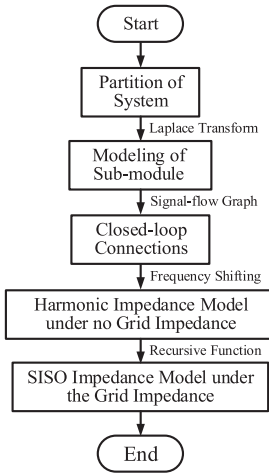
Fig. 10. Flowchart of the recursive impedance modeling method.

The recursive SISO impedance model has an analytical expression. Moreover, the recursive SISO impedance is easy to incorporate harmonics of arbitrary order by only four transfer functions ($Y_{op}(s)$, $Y_p(s)$, $Y_n(s)$, and $Y_g(s)$) with their frequency-shifting copies. In addition, the matrix inversion is avoided compared with [34]. When no grid impedance exists ($Z_g(s) = 0$), it yields $F_N(\bullet) = 0$ and $F_P(\bullet) = 0$ such that the recursive impedance $Z(s)$ degrades to $Z_{op}(s)$.

Overall, the recursive SISO impedance modeling method is summarized as Fig. 10, which includes two main steps. The first step is to establish the harmonic admittance model under no grid impedance condition, which can be deemed as the fundamental frequency coupling. The next step is to construct the complete system dynamics by frequency-shifting the fundamental frequency coupling, and then the recursive SISO impedance model can be derived based on the idea of mathematical induction.

Remark: Considering a multiphase system under linear grid impedance, the relationship between the voltage vector and the grid current vector in an *M*-phase system ($M \in \mathbb{N}^+$) can be expressed as

$$i\left(s_K\right) = \boldsymbol{Y}_0\left(s_K\right)\boldsymbol{u}\left(s_K\right) + \sum_{m=1}^{N_1} \boldsymbol{Y}_{\boldsymbol{pm}}\left(s_{K-m}\right)\boldsymbol{u}\left(s_{K-m}\right)$$
$$+ \sum_{l=1}^{N_2} \boldsymbol{Y}_{\boldsymbol{nl}}\left(s_{K+l}\right)\boldsymbol{u}\left(s_{K+l}\right) \qquad (66)$$

where $\boldsymbol{i}(s_K) = [i_1(s_K), i_2(s_K), ..., i_M(s_K)]^T$, $\boldsymbol{u}(s_K) = [u_1(s_K), u_2(s_K), ..., u_M(s_K)]^T$, $N_1 \in \mathbb{N}$, $N_2 \in \mathbb{N}$, and $K \in \mathbb{Z}$. And $\boldsymbol{Y}_{pK}$, $\boldsymbol{Y}_0$, and $\boldsymbol{Y}_{nK}$ are all definite *M*-by-*M* matrices.

The additional loop resulted from the grid admittance can be expressed as

$$i\left(s_K\right) = -\boldsymbol{Y}_g\left(s_K\right)\boldsymbol{u}\left(s_K\right) \qquad (67)$$

where $\boldsymbol{Y}_g(s_K) = \text{diag}[Y_{g1}(s_K), Y_{g2}(s_K), ..., Y_{gM}(s_K)]$ and $K \in \mathbb{Z} \backslash 0$.

The truncation conditions are expressed as

$$\begin{cases} \boldsymbol{u}\left(s_X\right) = 0, & X \geq P+1 \\ \boldsymbol{u}\left(s_{-Y}\right) = 0, & Y \geq N+1. \end{cases} \qquad (68)$$

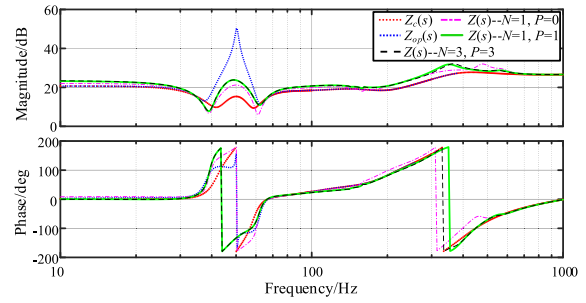Fig. 11. Comparative analysis of SISO impedance with different truncation orders under $L_g = 5.5$ mH and $R_g = 1.5$ Ω.

TABLE I
MAIN CIRCUIT AND CONTROL PARAMETERS

Symbol	Description	Value
u_g	Grid voltage	100 V(rms)
ω_1	Input angular frequency	100π rad/s
L_f	Input filter inductance	2.8 mH
R_f	Input filter resistance	0.1 Ω
C_{dc}	Output capacitance	240 μF
R_{dc}	Load resistance	62.5 Ω
ω_i/ω_v	ADC cutoff frequency	10^4π rad/s
ξ	Damping ratio of the SOGI	0.707
k_{p1}	Proportional gain of the PLL	6.3
k_{i1}	Integral gain of the PLL	7896
k_{p2}	Proportional gain of the voltage regulator	2.8×10^{-5}
k_{i2}	Integral gain of the voltage regulator	0.03
k_{pc}	Proportional gain of the current regulator	6.7
k_{rc}	Resonant gain of the current regulator	11640
ω_n	Center frequency of Notch filter	200π rad/s
σ	Bandwidth coefficient of Notch filter	4737
u_{dc}^*	Output voltage reference	250 V
T_s	Control period	50 μs

According to the idea of mathematical induction, two recursive relationships can be derived as

$$\boldsymbol{u}\left(s_K\right) = \sum_{m=1}^{N_1} \boldsymbol{F}_{pm}\boldsymbol{u}\left(s_{K-m}\right) \qquad (69)$$

$$\boldsymbol{u}\left(s_{-K}\right) = \sum_{l=1}^{N_2} \boldsymbol{F}_{nl}\boldsymbol{u}\left(s_{-K+l}\right) \qquad (70)$$

where $\boldsymbol{F}_{pm}$ and $\boldsymbol{F}_{nl}$ are two recursive functions.

Combining (66), (69), and (70) and performing the frequency-shifting, the relationship between $\boldsymbol{i}(s_0)$ and $\boldsymbol{u}(s_0)$ can be solved. Therefore, the developed recursive SISO modeling method has a great potential of being promoted to other time-periodic systems.

B. Frequency Response Analysis of Recursive Impedance

The model accuracy depends on the chosen truncation order. When finite-order truncation is performed, frequency response deviation may occur, as shown in Fig. 11 (main parameters are listed in Table I). The selection of truncation order mainly influences the frequency response of $Z(s)$ around the fundamental frequency. And the frequency response deviation decreases
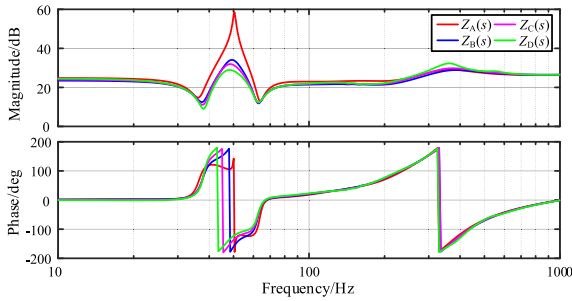
Fig. 12. Comparative analysis of SISO impedance with different grid impedances. $Z_A(s)$: $L_g = 0$ mH and $R_g = 0$ Ω; $Z_B(s)$: $L_g = 1.5$ mH and $R_g = 1$ Ω; $Z_C(s)$: $L_g = 3.5$ mH and $R_g = 1$ Ω; and $Z_D(s)$: $L_g = 5.5$ mH and $R_g = 1$ Ω.
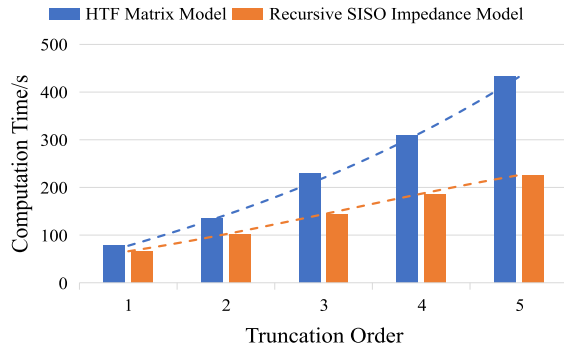

Fig. 13. Computation time comparisons of $Z_{\mathrm{HTF}}(s)$ and $Z(s)$ with different truncation orders.

as the truncation order increases. The evaluation of truncation order has also been discussed in the literature [34], but an explicit formula has not yet been provided. Thus, the truncation parameters P and N are usually evaluated iteratively. In the work presented in the following, $N = 3$ and $P = 3$ have been chosen.

In order to better visualize the influence of grid impedance, the impedance model $Z(s)$ under different grid impedances are plotted in Fig. 12. The symbol $Z_X(s)$ ($X = A, B, C, D$) are used to represent $Z(s)$ under different grid impedances ($Z_A(s)$: $L_g = 0$ mH, $R_g = 0$ Ω; $Z_B(s)$: $L_g = 1.5$ mH, $R_g = 1$ Ω; $Z_C(s)$: $L_g = 3.5$ mH, $R_g = 1$ Ω; $Z_D(s)$: $L_g = 5.5$ mH, $R_g = 1$ Ω). From Fig. 12, it is observed that evident discrepancies occur around the fundamental frequency as the grid impedance changes, which shows that the rectifier impedance depends on the grid impedance. There exist two valley points in the low-frequency regions, whose frequencies are symmetric about the fundamental frequency. And, with the increase of the grid impedance, the magnitude gain of the rectifier impedance decreases, implying that the ability to suppress voltage disturbances near the valley frequencies degrades.

Based on the MATLAB platform, the computation time required to calculate the impedance response of the HTF matrix-based model [34] and the proposed recursive SISO model at one thousand frequency points is shown in Fig. 13. As seen, the computation time required by the recursive SISO model is always less than that of the HTF matrix-based model, verifying the superiority of the recursive SISO model in the computational burden. The reason for the superiority lies in the elimination of large-dimensional matrix operations. The recursive SISO

model can save approximately 16.7% time when the truncation order is 1. Moreover, the polynomial fitting curve shows that the computation complexity of the HTF matrix-based model will increases exponentially as the truncation order increases. In contrast, the computation complexity of the recursive SISO model increases almost linearly as the truncation order increases.

C. Comparison Between the Existing Impedance Models and the Proposed Recursive Impedance Model

Many modeling methods can lead to accurate models, but their modeling procedures and the resulting models are different. Table II summarizes the comparison results of the existing impedance modeling methods and the proposed modeling method for the single-phase converters. As shown in Table II, the modeling methods can be mainly categorized into two types: describing-function-based methods and linearization-based methods.

The harmonic linearization modeling method and the harmonic signal-flow graph modeling method can be directly applied to the nonlinear time-periodic systems without linearization. However, the additional closed-loops caused by the grid impedance are neglected and complex convolutions are needed for the submodule modeling. The multifrequency modeling method, the HTF modeling method, and the proposed modeling method all directly linearize the nonlinear time-periodic system around ac steady-state trajectories. The multifrequency modeling method considers a limited number of frequency coupling loops, which may be a potential limitation for model accuracy. The use of large-dimensional matrices degrades model analyticity and increases the computation effort of the HTF model. The proposed recursive SISO impedance modeling method gives an analytical model, which can include the harmonics of arbitrary order with low computation burdens. Thus, it is a promising choice for single-phase converter modeling.

VI. EXPERIMENTAL VALIDATION

In this section, a prototype of the single-phase VSR is built to verify the correctness of the proposed models, as shown in Fig. 14. The system specifications are the same as Table I. The control platform is based on a floating-point digital signal processor (DSP) TMS320F28335. The grid voltage and the injected small perturbation from 10 Hz to 1 kHz are generated by a regenerative grid simulator (Chroma 61830). And the measured signals are sent to the frequency response analyzer Bode 100.

A. Frequency Scan Validation

The implementation of the impedance measurement scheme is depicted in Fig. 15. A small-signal perturbation voltage u_p is injected, which excites the perturbations of corresponding frequency on the PCC voltage and input current. The PCC voltage signal u_i sends to the CH1 port, and the grid current signal i_g transmits to the CH2 port. The measured impedance is obtained by plotting the bode diagram of CH1/CH2.

The frequency response characteristics of the built impedance models and the corresponding measured results under different

TABLE II
COMPARISON OF THE EXISTING IMPEDANCE MODELING METHODS AND THE PROPOSED MODELING METHOD FOR SINGLE-PHASE CONVERTERS

|	Harmonic linearization method[29]	Harmonic signal flow graph method[30]-[31]	Multi-frequency method[33]	Harmonic transfer function method[34]	Proposed method
Modeling object	PFC rectifier	PWM rectifier	PWM inverter	PWM rectifier	PWM rectifier
Frequency-coupling components	Diode bridge	PLL DC-link voltage	PLL	PLL DC-link voltage	PLL DC-link voltage
Submodule modeling	Describing function	Describing function	Transfer function vector	Transfer function matrix	Transfer function vector
Coupling frequencies	Arbitrary	$\omega\pm\omega_1$	ω $\omega\pm2\omega_1$	Arbitrary	Arbitrary
Grid impedance effect	Ignored	Ignored	Considered	Considered	Considered
Steady-state DC voltage trajectory	All	DC	/	All	All
Model analyticity	Good	Good	Good	Medium	Good
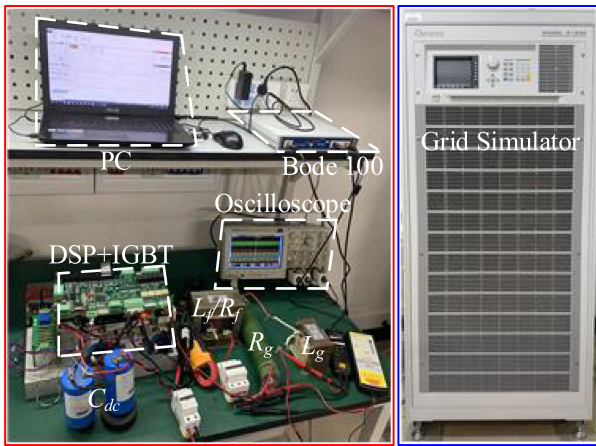
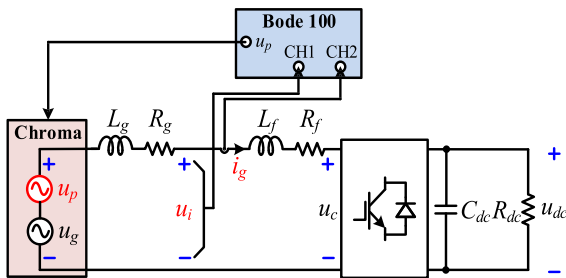Fig. 14. Experimental setup for SISO impedance measurement verification.

Fig. 15. Impedance measurement scheme for single-phase converters.

grid impedances are plotted in Fig. 16. As shown, the conventional impedance $Z_c(s)$, which only considers the fundamental perturbed components, has a large deviation in the regions around the fundamental frequency. The $Z_{\mathrm{op}}(s)$ achieves higher accuracy compared with $Z_c(s)$, but the accuracy degrades as the grid impedance increases. In contrast, the measured results are in good accordance with $Z(s)$, which validates the accuracy of the
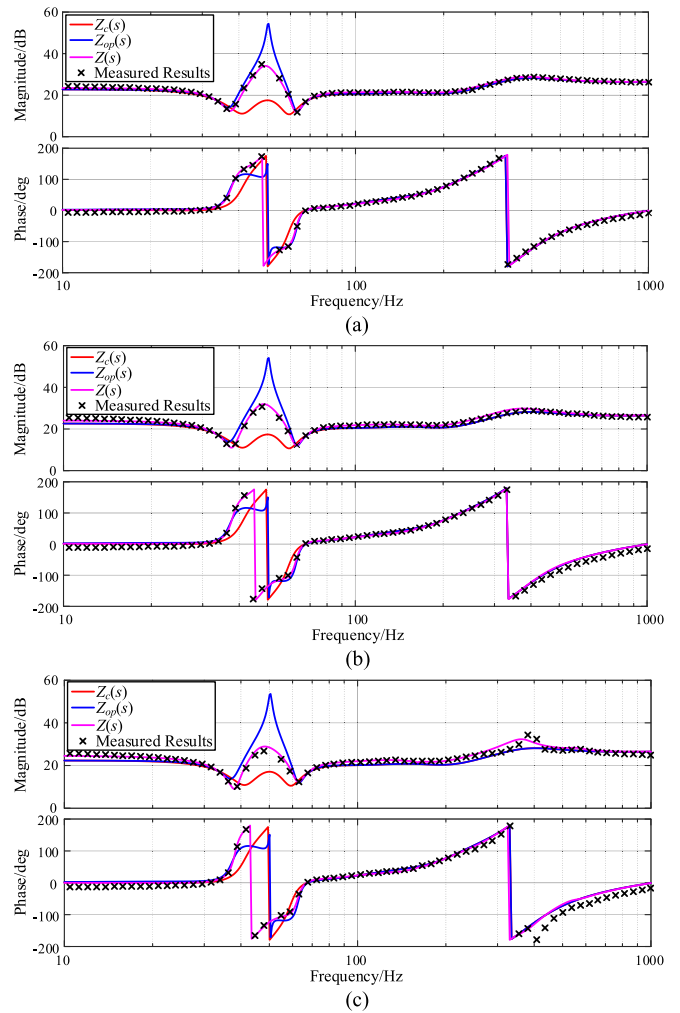

Fig. 16. Impedance responses. Solid lines: model prediction; dots: experimental results. (a) Case A: $(L_g, R_g) = (1.5\,\mathrm{mH}, 1)\,\Omega$. (b) Case B: $(L_g, R_g) = (3.5\,\mathrm{mH}, 1)\,\Omega$. (c) Case C: $(L_g, R_g) = (5.5\,\mathrm{mH}, 1)\,\Omega$.
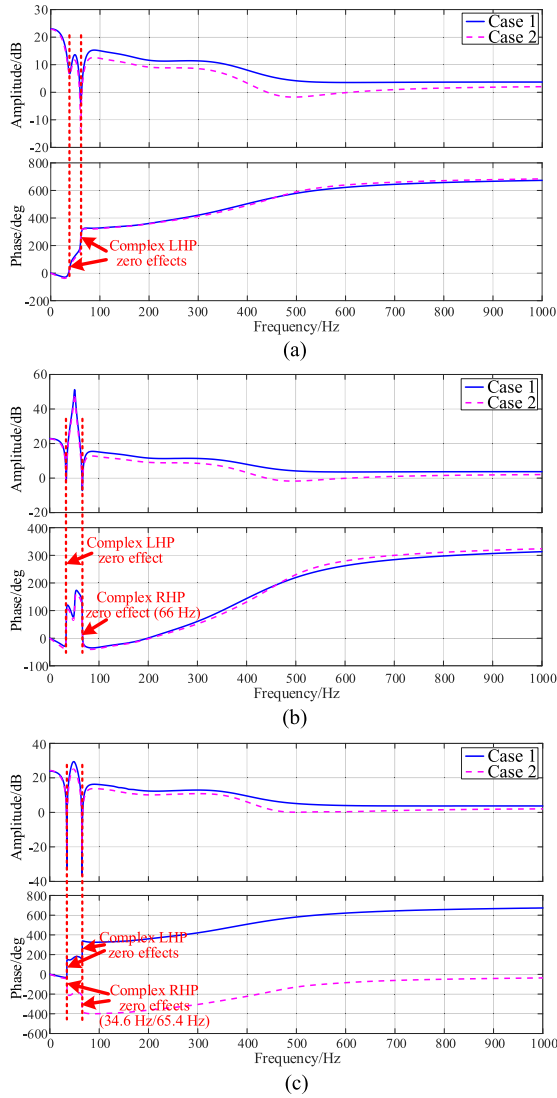
Fig. 17. Stability analysis with $1 + Z_Y(s)/Z_g(s)$, where $Z_Y = Z_c$, Z_{op}, and Z. (a) $1 + Z_c(s)/Z_g(s)$. (b) $1 + Z_{op}(s)/Z_g(s)$. (c) $1 + Z(s)/Z_g(s)$

proposed impedance modeling approach. Since some unmodeled perturbations (e.g., the nonlinearity of the passive components, precision of measurement device, parasitic parameters) exist in the actual experimental setup, there still exists a small deviation between the measured results and calculated results of $Z(s)$, which is a common problem in impedance measurement [30], [33].

The experimental measurement shows that the couplings between the grid impedance and the rectifier play an important role in the model accuracy. Thus, it is suggested that the interactions resulted from the grid impedance should be considered in the input impedance modeling of the single-phase VSR system.

B. Stability Analysis

This section will further analyze the validity of the proposed SISO models in terms of small-signal stability. The system stability is assessed by analyzing the zero effects of $1 + Z_Y(s)/Z_g(s)$ [28], [36], where $Z_Y = Z_c$, Z_{op}, and Z.

TABLE III
PERFORMANCES COMPARAISONS UNDER DIFFERENT Z_g

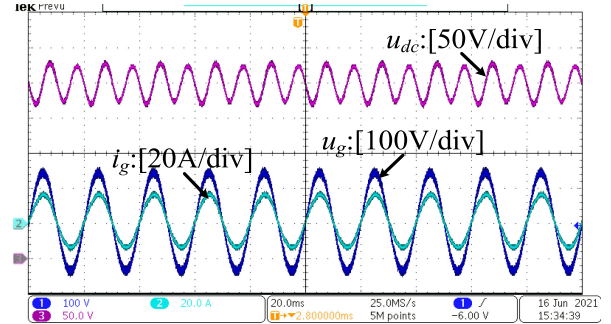| Model	Items	Case 1 (Z_g=3mH/1Ω)	Case 2 (Z_g=4.5mH/1Ω)
Z_c Fig. 17(a)	Stable	Yes	Yes
	Resonant frequency	/	/
Z_{op} Fig. 17(b)	Stable	No	No
	Resonant frequency	66 Hz	66 Hz
Z Fig. 17(c)	Stable	**Yes**	**No**
	Resonant frequency	/	34.6 Hz, 65.4 Hz

Fig. 18. Experimental waveforms under $Z_g = 3$ mH/1 Ω.

First, with a fixed voltage loop bandwidth $f_b = 21$ Hz, different SISO impedance models under $Z_g = 3$ mH/1 Ω (i.e., Case 1) and $Z_g = 4.5$ mH/1 Ω (i.e., Case 2) are compared in Fig. 17. The frequency response curves concerning Z_c and Z_{op} remain almost the same under different Z_g, and the small deviation is caused by the increased steady-state voltage drop across the grid impedance.

By analyzing Fig. 17(a), no right-half plane (RHP) zero effect is observed, indicating a stable system in both cases. On the contrary, both cases are predicted to be unstable by Z_{op} as shown in Fig. 17(b), where the complex RHP zero effect is found at 66 Hz. From 17(c), only complex left-half plane (LHP) zero effects are found in Case 1, indicating a stable system. While for Case 2, the complex RHP zero effects are found at 34.6 and 65.4 Hz, meaning that the system is unstable. The harmonic and stability identified by different models are summarized in Table III.

Experimental waveforms under Cases 1 and 2 are shown in Figs. 18 and 19. When $Z_g = 3$ mH/1 Ω, no unstable oscillation exists in both the grid current i_g and dc-link voltage u_{dc}. However, when the grid impedance Z_g increases to 4.5 mH/1 Ω, the grid current i_g and the dc-link voltage u_{dc} exhibit low-frequency oscillation, indicating an unstable system. By analyzing the spectrum of i_g, the oscillation frequencies of 34 and 66 Hz are all identified as shown in Fig. 19(b), which closely agrees with the analyzed results in Fig. 17(c). Based on the above discussion, the neglect of frequency couplings will lead to inaccurate stability results.

Further, the influence of voltage loop bandwidth f_b on the system stability is analyzed. Fig. 20 shows the frequency response curves of $1 + Z(s)/Z_g(s)$ under a fixed grid impedance
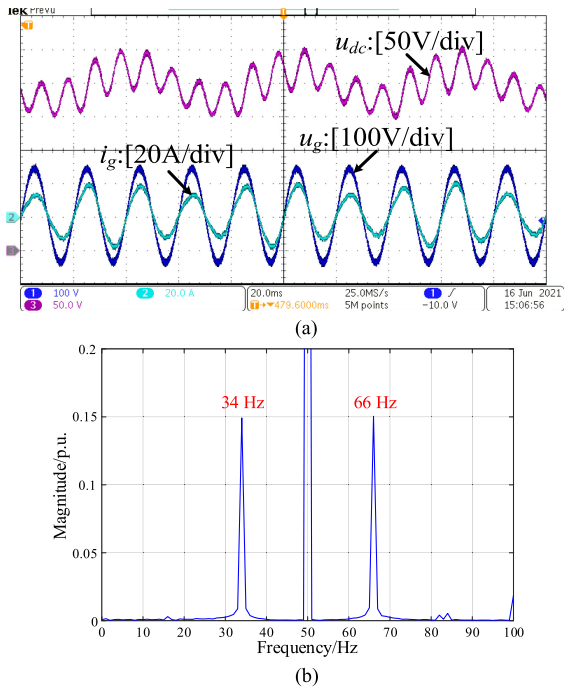
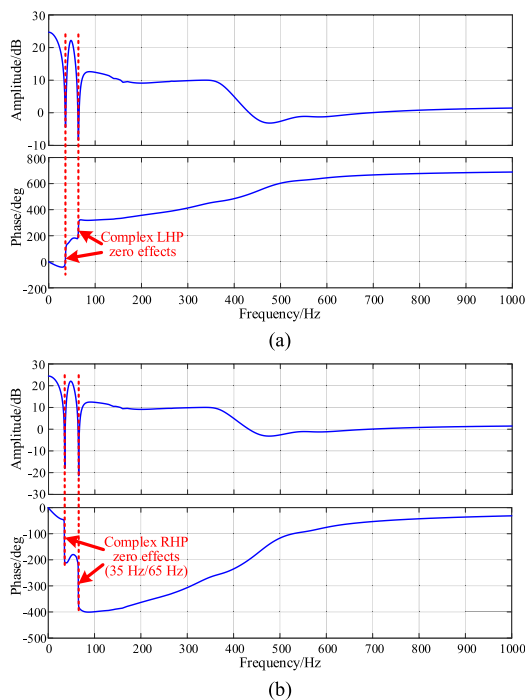Fig. 19. Experimental waveforms under $Z_g = 4.5$ mH/1 Ω. (a) Time-domain waveforms. (b) Spectrum of i_g.

Fig. 20. Stability analysis with $1 + Z(s)/Z_g(s)$. (a) Voltage control bandwidth $f_b = 19$ Hz. (b) Voltage control bandwidth $f_b = 21$ Hz.

TABLE IV
STABILITY ANALYSIS WITH DIFFERENT f_b

f_b	Stable	Resonant frequency
19 Hz (Fig. 20(a))	Yes	/
21 Hz (Fig. 20(b))	No	35 Hz, 65 Hz
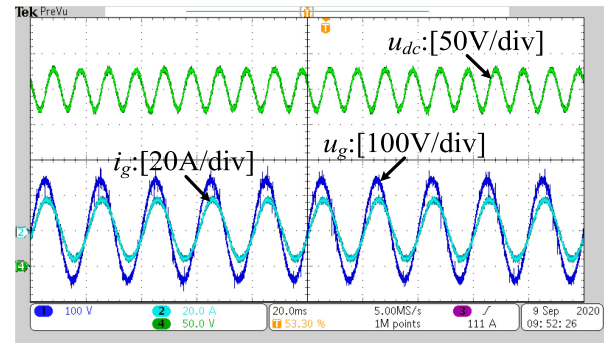
Fig. 21. Experimental waveforms with $f_b = 19$ Hz.
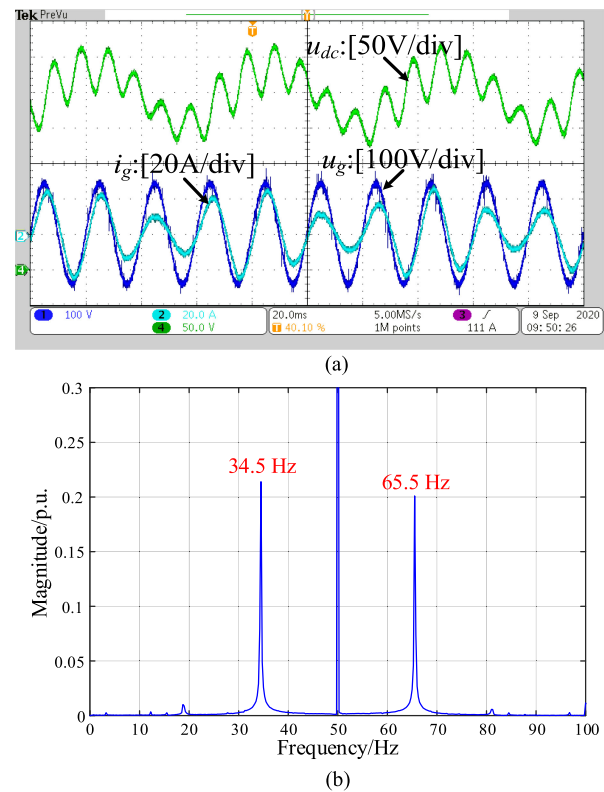
Fig. 22. Experimental waveforms with $f_b = 21$ Hz. (a) Time-domain waveforms. (b) Spectrum of i_g

harmonic and stability under different voltage loop bandwidths are summarized in Table IV.

Experiments are carried out with $f_b = 19$ Hz and $f_b = 21$ Hz in Figs. 21 and 22, respectively. It is seen that for $f_b = 19$ Hz, the grid current i_g remains sinusoidal and the average value of dc-link voltage u_{dc} tracks its reference, meaning that this system is stable. Whereas for $f_b = 21$ Hz, instability occurs that dc-link voltage u_{dc} and the grid current i_g oscillate with low

($L_g = 5.5$ mH, $R_g = 1$ Ω) when the voltage loop bandwidth f_b is configured as 19 and 21 Hz, respectively. According to Fig. 20(a), only complex LHP zero effects are found when $f_b = 19$ Hz, indicating a stable system. While for $f_b = 21$ Hz as shown in Fig. 20(b), the complex RHP zero effects are found at 35 and 65 Hz, implying that the system is unstable. The

frequency. The FFT analysis of i_g is shown in Fig. 22(b), where the oscillation frequencies of 34.5 and 65.5 Hz can be identified. Similarly, the observed oscillation frequencies closely agree with the analyzed results in Fig. 20.

The stability analysis demonstrates that the proposed impedance model is accurate for stability prediction. The impedance models Z_c and $Z_{\rm op}$ have limitations in stability analysis due to the neglect of FCEs. Additionally, the small-signal stability analysis shows that smaller grid impedance Z_g and lower voltage loop bandwidth f_b can achieve better stability in terms of the VSC-grid interaction. Increasing grid impedance Z_g or voltage loop bandwidth f_b will move two complex LHP zeros to the RHP, and thus the low-frequency oscillation occurs.

VII. Conclusion

In this article, a recursive SISO impedance modeling framework for the single-phase converters is proposed. Through the displacement property of the Laplace transform and the frequency-shifting operation, the traditional LTI modeling is extended to LTP modeling. The LTP modeling method transferred the time-varying model into a time-invariant transfer function vector model. The complex convolution and the Toeplitz matrix are eliminated in the submodule modeling, so the modeling complexity is reduced. Furthermore, based on the idea of mathematical induction, a recursive SISO impedance model can be obtained by solving the additional loops closed by the grid impedance. The recursive SISO impedance model is analytical and accurate. Moreover, compared with the HTF-matrix-based SISO impedance model, the recursive SISO impedance model has lower computation burdens.

On the other hand, it is found that both the increase of voltage loop bandwidth and grid impedance lead to low-frequency oscillations. Also, the typical impedance without considering any FCE is over-optimistic on the stability assessment, whereas the impedance neglecting the grid impedance effect is over-conservative in terms of stability. An accurate stability analysis must take all the frequency coupling components into account.

The proposed modeling method has a great potential of being promoted to other time-periodic systems. The detailed modeling and analysis of the multiphase system under complex grid conditions will be the topic of future research.

Appendix

The transfer function of the harmonic admittance model

$$G_{i,-2}(s) = -\frac{1}{2}G_d(s)\,\mathrm{PR}(s)\,G_{\rm in}(s) \tag{71}$$

$$G_{i,0}(s) = L_f s + R_f + G_d(s)\,\mathrm{PR}(s)\,G_{\rm si}(s)$$
$$-\frac{G_d(s)\,\mathrm{PR}(s)}{2}\left[G_{\rm ip}(s-j2\omega_1) + G_{\rm in}(s+j2\omega_1)\right] \tag{72}$$

$$G_{i,2}(s) = -\frac{1}{2}G_d(s)\,\mathrm{PR}(s)\,G_{\rm ip}(s) \tag{73}$$

$$G_{u,-2}(s) = \frac{G_d(s)\,\mathrm{PR}(s)}{2}\left[G_{\rm un}(s) + jI_1 G_{\mathrm{PLL\_}n}(s-j\omega_1)\right] \tag{74}$$

$$G_{u,0}(s) = 1 - G_d(s)\,G_{\rm sv}(s)$$
$$+\frac{jI_1 G_d(s)\,\mathrm{PR}(s)}{2}\left[G_{\mathrm{PLL\_}p}(s-j\omega_1) - G_{\mathrm{PLL\_}n}(s+j\omega_1)\right]$$
$$+\frac{G_d(s)\,\mathrm{PR}(s)}{2}\left[G_{\rm up}(s-j2\omega_1) + G_{\rm un}(s+j2\omega_1)\right] \tag{75}$$

$$G_{u,2}(s) = \frac{1}{2}G_d(s)\,\mathrm{PR}(s)\left[G_{\rm up}(s) - jI_1 G_{\mathrm{PLL\_}p}(s+j\omega_1)\right] \tag{76}$$

$$G_{\rm un}(s) = -I_1 e^{j\varphi_{i1}} G_{\rm vol}(s-j\omega_1) \tag{77}$$

$$G_{\rm up}(s) = -I_1 e^{-j\varphi_{i1}} G_{\rm vol}(s+j\omega_1) \tag{78}$$

$$G_{\rm in}(s) = -G_{\rm vol}(s-j\omega_1)\begin{bmatrix}V_1 - (s-j2\omega_1)L_f I_1 e^{j\varphi_{i1}}\\ -j\omega_1 L_f I_1 e^{j\varphi_{i1}} - 2R_f I_1 e^{j\varphi_{i1}}\end{bmatrix} \tag{79}$$

$$G_{\rm ip}(s)$$
$$= -G_{\rm vol}(s+j\omega_1)\begin{bmatrix}V_1 - (s+j2\omega_1)L_f I_1 e^{-j\varphi_{i1}}\\ +j\omega_1 L_f I_1 e^{-j\varphi_{i1}} - 2R_f I_1 e^{-j\varphi_{i1}}\end{bmatrix} \tag{80}$$

$$G_{\rm vol}(s) = H_v(s)\,G_L(s). \tag{81}$$

References

[1] F. Blaabjerg, R. Teodorescu, M. Liserre, and A. V. Timbus, "Overview of control and grid synchronization for distributed power generation systems," *IEEE Trans. Ind. Electron.*, vol. 53, no. 5, pp. 1398–1409, Oct. 2006.

[2] E. Mollerstedt and B. Bernhardsson, "Out of control because of harmonics-an analysis of the harmonic response of an inverter locomotive," *IEEE Control Syst. Mag.*, vol. 20, no. 4, pp. 70–81, Aug. 2000.

[3] L. Zhang, L. Harnefors, and H.-P. Nee, "Interconnection of two very weak AC systems by VSC-HVDC links using power-synchronization control," *IEEE Trans. Power Syst.*, vol. 26, no. 1, pp. 344–355, Feb. 2011.

[4] X. Wang and F. Blaabjerg, "Harmonic stability in power electronic-based power systems: Concept, modeling, and analysis," *IEEE Trans. Smart Grid*, vol. 10, no. 3, pp. 2858–2870, May 2019.

[5] D. Yang, X. Wang, F. Liu, K. Xin, Y. Liu, and F. Blaabjerg, "Symmetrical PLL for SISO impedance modeling and enhanced stability in weak grids," *IEEE Trans. Power Electron.*, vol. 35, no. 2, pp. 1473–1483, Feb. 2020.

[6] A. Rygg, M. Molinas, C. Zhang, and X. Cai, "A modified sequence-domain impedance definition and its equivalence to the dq-domain impedance definition for the stability analysis of AC power electronic system," *IEEE J. Emerg. Sel. Topics Power Electron.*, vol. 4, no. 4, pp. 1383–1396, Dec. 2016.

[7] L. Harnefors, M. Bongiorno, and S. Lundberg, "Input-admittance calculation and shaping for controlled voltage-source converters," *IEEE Trans. Ind. Electron.*, vol. 54, no. 6, pp. 3323–3334, Dec. 2007.

[8] M. K. Bakhshizadeh *et al.*, "Couplings in phase domain impedance modeling of grid-connected converters," *IEEE Trans. Power Electron.*, vol. 31, no. 10, pp. 6792–6796, Oct. 2016.

[9] S. Shah and L. Parsa, "Impedance modeling of three-phase voltage source converters in dq, sequence, and phasor domains," *IEEE Trans. Energ. Conv.*, vol. 32, no. 3, pp. 1139–1150, Sep. 2017.

[10] X. Wang, L. Harnefors, and F. Blaabjerg, "Unified impedance model of grid-connected voltage-source converters," *IEEE Trans. Power Electron.*, vol. 33, no. 2, pp. 1775–1787, Feb. 2018.

[11] M. Belkhayat, "Stability criteria for AC power systems with regulated loads," Ph.D. dissertation, Purdue Univ., West Lafayette, IN, USA, Dec. 1997.

[12] L. Harnefors, M. Bongiorno, and S. Lundberg, "Input-admittance calculation and shaping for controlled voltage-source converters," *IEEE Trans. Ind. Electron.*, vol. 54, no. 6, pp. 3323–3334, Dec. 2007.

[13] B. Wen, D. Boroyevich, R. Burgos, P. Mattavelli, and Z. Shen, "Analysis of d-q small-signal impedance of grid-tied inverters," *IEEE Trans. Power Electron.*, vol. 31, no. 1, pp. 675–687, Jan. 2016.

[14] L. Harnefors, "Modeling of three-phase dynamic systems using complex transfer functions and transfer matrices," *IEEE Trans. Ind. Electron.*, vol. 54, no. 4, pp. 2239–2248, Aug. 2007.

[15] C. Zhang, X. Cai, A. Rygg, and M. Molinas, "Sequence domain SISO equivalent models of a grid-tied voltage source converter system for small-signal stability analysis," *IEEE Trans. Energ. Conv.*, vol. 33, no. 2, pp. 741–749, Jun. 2018.

[16] J. Liu, X. Du, Y. Shi, and H.-M. Tai, "Impedance measurement of three-phase inverter in the stationary frame using frequency response analyzer," *IEEE Trans. Power Electron.,* vol. 35, no. 9, pp. 9390–9401, Sep. 2020.

[17] D. Yang and X. Wang, "Unified modular state-space modeling of grid-connected voltage-source converters," *IEEE Trans. Power Electron.,* vol. 35, no. 9, pp. 9700–9715, Sep. 2020.

[18] S. R. Sanders, J. M. Noworolski, X. Z. Liu, and G. C. Verghese, "Generalized averaging method for power conversion circuits," *IEEE Trans. Power Electron.*, vol. 6, no. 2, pp. 251–259, Apr. 1991.

[19] A. M. Stankovic, S. R. Sanders, and G. C. Verghese, "Dynamic phasors in modeling and analysis of unbalanced polyphaser ac machines," *IEEE Trans. Energy Conv.*, vol. 17, no. 1, pp. 107–113, Mar. 2002.

[20] S. Lissandron, L. Santa, P. Mattavelli, and B. Wen, "Experimental validation for impedance-based small-signal stability analysis of single-phase interconnected power systems with grid-feeding inverters," *IEEE J. Emerg. Sel. Topics Power Electron.*, vol. 4, no. 1, pp. 103–115, Mar. 2016.

[21] N. M. Wereley, "Analysis and control of linear periodically time varying systems," Ph.D. dissertation, Dept. Aeronautics and Astronautics, MIT Inst. Technol.,Cambridge, MA, USA, 1991.

[22] J. B. Kwon, X. Wang, F. Blaabjerg, C. L. Bak, A. R. Wood, and N. R. Watson, "Harmonic instability analysis of a single-phase grid-connected converter using a harmonic state-space modeling method," *IEEE Trans. Ind. Appl.*, vol. 52, no. 5, pp. 4188–4200, Sep. 2016.

[23] J. B. Kwon, X. Wang, F. Blaabjerg, C. L. Bak, V. S. Sularea, and C. Busca, "Harmonic interaction analysis in a grid-connected converter using harmonic state-space (HSS) modeling," *IEEE Trans. Power Appl.*, vol. 32, no. 9, pp. 6823–6835, Sep. 2017.

[24] V. Salis, A. Costabeber, S. M. Cox, P. Zanchetta, and A. Formentini, "Stability boundary analysis in single-phase grid-connected inverters with PLL by LTP theory," *IEEE Trans. Power Electron.,* vol. 33, no. 5, pp. 4023–4036, May. 2018.

[25] V. Salis, A. Costabeber, S. M. Cox, and P. Zanchetta, "Stability assessment of power-converter-based AC systems by LTP theory: Eigenvalue analysis and harmonic impedance estimation," *IEEE J. Emerg. Sel. Topics Power Electron.,* vol. 5, no. 4, pp. 1513–1525, Dec. 2017.

[26] E. Mollerstedt, "Dynamic analysis of harmonics in electrical systems," Ph.D. dissertation, Dept. Automatic Control, Lund Inst. Technol., Lund, Sweden, 2000.

[27] C. Zhang, M. Molinas, A. Rygg, J. Lyu, and X. Cai, "Harmonic transfer-function-based impedance modeling of a three-phase VSC for asymmetric AC grids stability analysis," *IEEE Trans. Power Electron.*, vol. 34, no. 12, pp. 12552–12566, Dec. 2019.

[28] Y. Liao, X. Wang, X. Yue, and L. Harnefors, "Complex-valued multi-frequency admittance model of three-phase VSCs in unbalanced grids," *IEEE J. Emerg. Sel. Topics Power Electron.*, vol. 8, no. 12, pp. 1934–1946, Jun. 2020.

[29] J. Sun and K. Karimi, "Small-signal input impedance modeling of line-frequency rectifiers," *IEEE Trans. Aerosp. Electron. Syst.*, vol. 44, no. 4, pp. 1489–1497, Oct. 2008.

[30] H. Zhang, Z. Liu, S. Wu, and Z. Li, "Input impedance modeling and verification of single-phase voltage source converters based on harmonic linearization," *IEEE Trans. Power Electron.*, vol. 34, no. 9, pp. 8544–8554, Sep. 2019.

[31] S. Shah and L. Parsa, "On impedance modeling of single-phase voltage source converters," in *Proc. IEEE Energy Conv. Cong. Expo.*, 2016, pp. 1–8.

[32] S. Shah, P. Koralewicz, V. Gevorgian, and L. Parsa, "Small-signal modeling and design of phase-locked loops using harmonic signal-flow graphs," *IEEE Trans. Energy. Conv.*, vol. 35, no. 2, pp. 600–610, Jun. 2020.

[33] Q. Qian, S. Xie, J. Xu, K. Xu, S. Bian, and N. Zhong, "Output impedance modeling of single-phase grid-tied inverters with capturing the frequency-coupling effect of PLL," *IEEE Trans. Power Electron.*, vol. 35, no. 5, pp. 5479–5495, May 2020.

[34] C. Zhang, M. Molinas, S. Foyen, J. A. Suul, and T. Isobe, "Harmonic domain SISO equivalent impedance modeling and stability analysis of a single-phase grid connected VSC," *IEEE Trans. Power Electron.*, vol. 35, no. 9, pp. 9770–9783, Sep. 2020.

[35] J. Borwein, D. Bailey, and R. Girgensohn, *Experimentation in Mathematics: Computational Paths to Discovery*. Natick, MA, USA: A K Peters. 2004.

[36] Y. Liao and X. Wang, "Impedance-based stability analysis for interconnected converter systems with open-loop RHP poles," *IEEE Trans. Power Electron.*, vol. 35, no. 4, pp. 4388–4397, Apr. 2020.

Jianheng Lin was born in Fujian, China, in 1994. He received the B.S. degree in electronic engineering from Jimei University, Xiamen, China, in 2016. He is currently working toward the Ph.D. degree in control science and engineering with the Central South University, Changsha, China.

His research interests include modeling, analysis, and control of power electronic systems.

Mei Su (Member, IEEE) was born in Hunan, China, in 1967. She received the B.S., M.S., and Ph.D. degrees from the School of Information Science and Engineering, Central South University, Changsha, China, in 1989, 1992, and 2005, respectively.

She has been a Full Professor with the School of Automation, Central South University. Her research interests include matrix converter, adjustable speed drives, and wind energy conversion system.

Dr. Su is currently an Associate Editor for the IEEE TRANSACTIONS ON POWER ELECTRONICS.

Yao Sun (Member, IEEE) was born in Hunan, China, in 1981. He received the B.S., M.S., and Ph.D. degrees from Central South University, Changsha, China, in 2004, 2007, and 2010, respectively.

He has been a Professor with the School of Automation, Central South University. His research interests include matrix converter, microgrid, and wind energy conversion system.

Dongsheng Yang (Senior Member, IEEE) received the B.S., M.S., and Ph.D. degrees in electrical engineering from Nanjing University of Aeronautics and Astronautics, Nanjing, China, in 2008, 2011, and 2016, respectively.

In 2016, he joined Aalborg University, Aalborg, Denmark as a Postdoc Researcher, where he became an Assistant Professor with the Department of Energy Technology in 2018. Since 2019, he has been working within the Electrical Energy Systems group with Eindhoven University of Technology (TU/e), Eindhoven, The Netherlands, as an Assistant Professor. His main research interests include modeling, analysis, and control of large-scale power electronics-based power system, and advanced power conversion technologies for renewable energy generation and various industrial electrifications.

Shiming Xie was born in Fujian, China, in 1995. He received the B.S. degree in electronic engineering from Central South University, Changsha, China, in 2017. He is currently working toward the Ph.D. degree in control science and engineering at the Central South University, Changsha.

His research interests include matrix converter and modeling and control of power electronics converters.